Journal of Alloys and Compounds 824 (2020) 153958

Contents lists available at ScienceDirect

Journal of Alloys and Compounds

journal homepage: http://www.elsevier.com/locate/jalcom

Ultrafine Cu_6Sn_5 nanoalloys supported on nitrogen and sulfur-doped carbons as robust electrode materials for oxygen reduction and Li-ion battery

Xiaoying Zhang , Luyao Liu , Jiaxin Liu , Tingting Cheng , Aiguo Kong *, Yu Qiao , Yongkui Shan **

School of Chemistry and Molecular Engineering, East China Normal University, Shanghai, 200241, China

ARTICLE INFO

Article history:
Received 22 August 2019
Received in revised form
13 January 2020
Accepted 20 January 2020
Available online 22 January 2020

Keywords:
Ultrafine particles
Cu_6Sn_5 nanoalloys
Oxygen reduction reaction
Li-ion battery

ABSTRACT

Ultrafine Cu_6Sn_5 nanoalloys supported on porous N and S-doped carbons (Cu_6Sn_5@N–S–Cs) were prepared by annealing Cu–Sn-contained covalent organic frameworks (COFs). The Cu_6Sn_5 alloys with particle size of about 2–10 nm were formed on the surface of N–S–Cs in a high dispersion state. The Cu_6Sn_5@N–S–Cs were found to efficiently catalyze oxygen reduction reaction (ORR) in both alkaline and acidic media, with half-wave ORR potential ($E_{1/2}$) of 0.86 V in 0.1 M KOH and 0.67 V in 0.1 M $HClO_4$. The ORR performance of Cu_6Sn_5@N–S–C could be competitive to the best Fe (or Co)-based non-precious metal electrocatalysts and commercial Pt/C. Cu_6Sn_5@N–S–C also showed better durability for ORR in both media. Moreover, Cu_6Sn_5@N–S–C also possessed electrochemical lithium ion storage capacity of 905 mA h g^{-1} in an initial discharge at the current density of 50 mA g^{-1}, with the outstanding coulomic efficiency. The synergistic effects of ultrafine Cu_6Sn_5 nanoalloys and porous N–S–Cs contributed to the impressive ORR performance and lithium storage capacities. COFs-derived Cu_6Sn_5@S–N–C was demonstrated to be a promising bifunctional electrode material for proton exchange membrane fuel cells and lithium ion batteries.

1. Introduction

The ever-increasing environmental problems arising from combustion of the nonrenewable fossil fuels have prompted global efforts to exploit renewable and sustainable energy storage and conversion techniques [1–3]. Among the developed energy conversion and storage systems, low-temperature proton exchange membrane fuel cells (PEMFCs) and lithium-ion batteries (LIBs) are especially attracting [4,5]. Electrochemical fuel cells could efficiently converse easily-transported small molecules like O_2, H_2, H_2O into powerful electrical energy [6]. Lithium-ion batteries with high energy densities were commercially available energy storage techniques in various devices including popular electronics vehicles [7]. For outputting power with higher efficiency, the continuous optimization of their structures and electrode materials was still required. High-performance electrode materials for speeding up oxygen reduction reaction (ORR) in PEMFCs and efficiently hosting lithium-ion storage in LIBs are the keys for enhancing the capacities of these two techniques [8]. Recently, the strongly supported hybrid materials of alloys and carbon supports have attracting more attention. The tight junction of alloys and carbons might arouse charge redistributions between their interfaces and produce new active catalytic species for ORR [9]. The alloy particles supported on carbons also led to the controlled size of alloys [10], which might facilitate the mass and electron exchanges of alloys and substances in electrolytes of fuel cells and LIBs. More importantly, longer time durability and cycle performance for ORR and lithium-ion storage in fuel cells and LIBs. The “so-called” synergistic effects make alloy@carbon hybrid materials been the potential electrode materials for ORR and lithium-ion storage.

The Pt-based alloys and non-precious Fe- or Co-based alloys supported on specific carbon supports have testified the outstanding ORR catalytic performance in wide pH electrolytes [11–13]. However, Cu–Sn-based alloys, manufacturing bronze in ancient China, are very scarce for efficiently catalyzing ORR, although they possess better affinity to O_2 and electron transfer

* Corresponding author.
** Corresponding author.
E-mail address: agkong@chem.ecnu.edu.cn (A. Kong).

https://doi.org/10.1016/j.jallcom.2020.153958
0925-8388/

properties [14]. Owing to the redox activities of Cu and Sn in electrolytes [15], Cu- and Sn-based electrode materials frequently fall into trouble in the capacity degradation. In particular, the small-size of CuSn alloys was often difficult to control, because the larger liquid droplets of Sn at higher temperature easily resulted into large-size particles of CuSn alloys [16]. This would lead to the weak synergistic effects between CuSn alloys and carbon supports and thus unsatisfactory ORR performance. On the other hand, CuSn alloys such as Cu_6Sn_5 have been investigated as the efficient anode materials in LIBs [17–19]. Cu_6Sn_5 possessed the large theoretical capacity of 605 mA h g^{-1} [20]. Although metallic Cu was inactive for lithium-ion storage, the formation of CuSn alloys could decrease the serious capacity decay from the volume expansion effect of Sn and effectively improved cycle performance of Sn-based anodes [21]. The smaller size of Cu_6Sn_5 alloys could further better accommodate the strain and relieve the pulverization of the active materials [22]. It also facilitated the lithation/de-lithation of Li^+ in intermetallic Cu_6Sn_5. The small-size Cu_6Sn_5 alloys strongly supported on special carbon supports could be utilized as the advanced bifuntional electrode materials for fuel cells and LIBs.

Covalent organic frameworks (COFs) emerged as a novel class of covalent polymer networks, consisting of lightweight elements (such as C, O, N, and S) [23,24]. The metallization of COFs could be achieved by grafting or introducing a few metal species in their porous frameworks [6]. Very recently, thermal conversion of these metal-modified COFs has been developed as a unique strategy to obtain carbon-based hybrid materials [25]. The organic frameworks easily derived the porous carbon skeletons with better mass-transportation properties, together with abundant doping heteroatoms. The metal species could often be conversed to the nanoparticles with the controlled size, which tightly encased or encapsulated by the derived carbon supports [26]. The strong synergistic effects between small-size nanoparticle and carbon supports enabled them to be the robust multifunctional electrode materials in energy conversion and storage [27,28]. The carbon-coupled FeN_x, FeP, FeC_x, FeS, CoN_x, CuFe and CoNi from the pyrolyzation of specific COFs have been reported as highly active ORR electrocatalysts [29–35]. The size of these nanoparticles could usually be 10–50 nm at the optimizing conditions. Conversion of the metal-modified COFs has shown their advantages in the production of d-block metal@carbon hybrid materials [36]. This strategy may be also feasible to synthesize small-size hybrid materials of ds- or p-block metal@carbons such as CuSn alloy@-carbons, though few reports about it.

Herein, ultrafine Cu_6Sn_5 nanoalloys have been successfully prepared by directly conversing Cu–Sn-contained COFs at higher temperature (Fig. 1). The formed Cu_6Sn_5 particles of about 2–10 nm were strongly supported on organic frameworks-carbonized porous N and S-doped carbons (N–S–Cs). The Cu_6Sn_5@N–S–Cs efficiently catalyzed ORR in 0.1 M KOH with half-wave potential ($E_{1/2}$) of 0.86 V, competitive to the best Fe (or Co)-based electrocatalysts. Cu_6Sn_5@S–N–C-900 also gave an initial discharge of 905 mA h g^{-1}, with a high coulombic efficiency (about 99%). Cu_6Sn_5@N–S–C hybrid materials testified the enhanced durability for ORR in aqueous electrolytes and cycle performance in lithium ions storage.

2. Experimental

2.1. Synthesis of Cu–Sn-COFs and Cu_6Sn_5@S–N–C catalysts

The as-synthesized 5, 10, 15, 20-tetrakis (4-aminophenyl) porphyrin (TAPP) containing Sn hydroxides (TAPP/$Sn(OH)_x$) was directly used as the raw regent (The synthesis details were given in Electronic Supporting Information(ESI)). 1.1 g of TAPP/$Sn(OH)_x$ and 0.42 g of 2,6-pyridinedicarboxaldehyde (PCBA) were added in dimethyl sulfoxide (DMSO, 50 mL) under N_2 atmosphere, with 4 ml of acetic acid in solution as the catalysts. An ethanol solution (10 ml) containing 0.75 g of Cu chloride dihydrate was subsequently injected into the above solution. The reaction mixtures were stirred and heated at 60 °C for 15 h in N_2. The cooled mixtures were filtered and washed with methanol. The Cu–Sn-contained porphyrin-based COFs (Cu–Sn-COFs) were finally collected as red powder. In addition, Cu-COFs and Sn-COFs were also prepared using the similar preparation procedures.

The as-prepared Cu–Sn-COFs were heated at 800–1000 °C for 4 h with a heating rate of 2 °C min^{-1} in N_2 atmosphere. The carbonized samples were leached in 0.2 M potassium hydroxide solution at room temperature for removing the excessive or instable Sn-based species. The final samples were labeled as Cu_6Sn_5@S–N–C-n (n is the pyrolyzation temperature). The single metal catalysts named as $Cu_{1.92}S$@S–N–C-900 and Sn@S–N–C-900 was also prepared using the same method.

2.2. Characterization

Solid ^{13}C NMR of TAPP were acquired on German Bruker Avance III 400 MHz nuclear magnetic resonance instrument. Powder X-ray diffraction (XRD) was performed on a D8 Advance X-ray diffractometer (Bruker AXS, Germany, Cu Kα), with a 2θ range of 10–80°. N_2 adsorption/desorption measurements were measured on the Quadra orb Evo Analyser at 77 K. The surface species analysis was investigated by X-ray photoelectron spectroscopy (XPS) with Al Kα radiation (15 kV, 150 W) on Axis Ultra DLD. Fourier transform infrared (FT-IR) spectra were recorded on infrared spectrophotometer of Bruker Tensor 27 in KBr pellets. The morphologies were observed with Hitachi S-4800 scanning electron microscope (SEM). The microstructures of all materials were observed with JEM-2100F transmission electron microscope (TEM). The HAADF-STEM was carried out using FEI-F30 TEM. Raman spectra were recorded using a GX-PT-1500 (150) apparatus with a 532 nm excitation laser. Supported plasma-atomic emission spectrometry (ICP-AES, IRIS Intrepid II) was employed to determine the metal content.

2.3. ORR electrochemical experiment

The ORR and methanol resistance performance of Cu_6Sn_5@S–N–Cs were examined at CHI–800C electrochemical working station in a three-electrode system. The Ag/AgCl (3 M) electrode, Pt wire electrode and rotating ring disk electrode (RRDE, 5 mm, Pine) were used as the reference electrode, the counter electrode and working electrode, respectively. The working electrode was prepared by dripping 10 μL ink on polished Glassy carbon electrode, and the ink was prepared by dispersing 10 mg Cu_6Sn_5@S–N–Cs in 1.25 mL ethanol with 30 μL of 5 wt% Nafion-2-propanol solution.

The ORR performance of Cu_6Sn_5@S–N–Cs was evaluated using cyclic voltammetry (CV) and rotated ring disk electrode (RRDE) techniques, with a scan rate of 5 mV s^{-1}. The electrolytes are O_2-saturated 0.1 M KOH and 0.1 M $HClO_4$ solution. Like the reported usage of Fe- or Co-based catalysts in literature [37,38], the catalyst loading of Cu_6Sn_5@S–N–Cs on the working electrodes was optimized to be 0.30 mg cm^{-2} in 0.1 M KOH and 0.60 mg cm^{-2} in 0.1 M $HClO_4$. For Pt/C, the value is 0.1 mg cm^{-2} in both electrolytes. All potentials were calibrated to the reversible hydrogen electrode (RHE) potentials (Fig. S1). The Koutecky-Levich (K-L) equations were used to calculate the kinetic parameters for the ORR. The Linear sweep voltammetry (LSV) curves were re-plotted as overpotential (η) versus log current (log j) to get Tafel plots for quantification of ORR kinetics. By fitting the linear part of Tafel plots, the

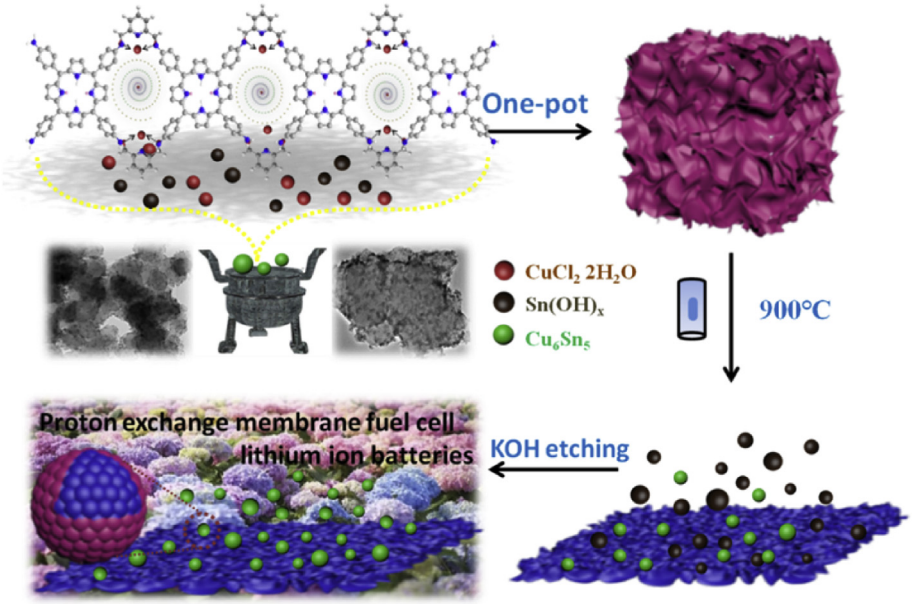

Fig. 1. Schematic representation for the synthesis of Cu_6Sn_5@S–N–C-900 electrocatalysts.

Tafel slope (b) and the exchange current density (J_0) was got from the Tafel equations ($\eta = a+b\log(j)$, $\log J_0 = -a/b$).

2.4. Li-ions battery

The Cu_6Sn_5@S–N–C-900 was assembled in a CR 2032-type coin cell. Super P carbon and poly (vinylidene fluoride) (PVDF) binder were mixed with Cu_6Sn_5@S–N–C-900 to form slurry at the weight ratio of 10:10:80. The anode was prepared by casting the slurry onto Cu foil using a doctor blade, and then dried in a vacuum oven at 120 °C overnight. The anode was cut into circular pieces with 1.0 cm diameter and the loading content is about 1.0 mg cm^{-2} for coin-cell testing. An ethylene carbonate-dimethyl carbonate (1:1 in volume) solution of $LiPF_6$ (1.0 M) soaking in a Whatman separator was used as the electrolyte and a lithium-metal foil as the counter electrode. The electrochemical tests were performed at various current densities (50, 100, 200, 400, 800, and 1600 mA g^{-1}) within 0.01–1.5 V voltage limit [39].

3. Results and discussion

3.1. Synthesis of Cu–Sn–COF precursor

The organic frameworks of as-prepared COFs were confirmed by solid-state ^{13}C NMR spectroscopy (See details in ESI Fig. S2A). The appearance state of Sn and Cu species in the Cu–Sn-COFs was detected with XPS and FT-IR (Fig. 2A). The Sn 3d spectra (Fig. 2B) could be deconvoluted into a doublet peak at 488.1 ($3d_{5/2}$) and 496.5 eV ($3d_{3/2}$), attributing to $Sn(OH)_x$ species in the Cu–Sn-COFs [40]. $SnCl_2$ was originally used as reduction agent in the synthesis of TAPP, finally remaining COFs in the hydrolysis form of $Sn(OH)_x$. The Cu 2p XPS spectrum (Fig. 2C) showed obvious characteristic peaks of Cu $2p_{3/2}$, satellite and Cu $2p_{1/2}$ at 930–960 eV [36], corresponding to Cu (II) and Cu (I) states. The strong adsorption peak at 1010 cm^{-1} in the FT-IR spectroscopy (Fig. 2A) suggested the existence of N-coordinated Cu-N_x in Cu–Sn-COFs [41]. The N 1s spectrum (Fig. 2D) was deconvoluted into two distinctive peaks at 401 and 399 eV. The former was assigned to the generation of N species bonded to Cu ions, and the later should be the pyrrole N of organic frameworks [42]. There was a clear XPS signal at 168 eV corresponding to S species in Cu–Sn-COFs (Fig. 2E). These S species should be left from the DMSO solvent, by coordinating with Cu and Sn ions or trapping in COFs. These results demonstrated that Cu and Sn metal-based species have been introduced into porphyrin-based organic skeletons containing abundant N and S non-metal species.

The amorphous phase structure of the as-prepared Cu–Sn-COFs was confirmed by a broad diffraction peak in the corresponding XRD patterns (Fig. S2B). The plate morphology of Cu–Sn-COFs was observed in SEM images (Fig. S3A). After looking carefully at these particles by TEM images (Figs. S3B and C), some irregular particles ascribing to Cu or Sn-contained particles were attached on the surface of COF plates. Cu–Sn-COFs showed a lower Bruauer-Emmett-Teller specific surface area (S_{BET}) of 162 m^2 g^{-1} than the COFs (394 m^2 g^{-1}) without Cu and Sn species (Fig. 2F). The decreased surface area might result from the pore blockage in COFs or the increased mass of COFs in unit volume after introducing Cu and Sn species. N_2 adsorption-desorption analysis also demonstrated a hierarchical porosity of the prepared COFs. The synthesized porous Cu–Sn-COFs with abundant N and S components served as the promising precursors to yield small-size Cu_6Sn_5 nanoalloys supported on N and S codoped carbons.

3.2. Structure and morphology of Cu_6Sn_5@S–N–C

After carbonizing Cu–Sn-COFs, the unique Cu_6Sn_5@S–N–Cs were successfully obtained. The formation of Cu_6Sn_5 nanoalloys (JSPDF No.45–1488) was firstly proved by the XRD pattern of Cu_6Sn_5@S–N–C-900, judged from the diffraction peaks occurring at $2\theta = 31.5$ (221), 42.9 (132), 43.2 (42–2), 53.3 (24–1), 56.6 (530), 60.0 (62–3), 62.6 (44–2), 70.8 (351), 74.3 (–733), 76.6 (64–3), and 78.8° (060) (Fig. 3A). Cu_6Sn_5@S–N–C displayed the stronger diffraction signals of Cu_6Sn_5 as the temperature increased. Cu_6Sn_5@S–N–C prepared at higher thermal-treatment temperatures would possess higher crystallinity or larger particle size. The content of Sn and Cu in Cu_6Sn_5@S–N–C-900 was about 18.7 and 8.3 wt%, determined by ICP-AES analysis. TEM images of Cu_6Sn_5@S–N–C-900 revealed lots of ultrafine irregular nanoparticles, highly dispersing on porous carbon plates (Fig. 4a-c). A

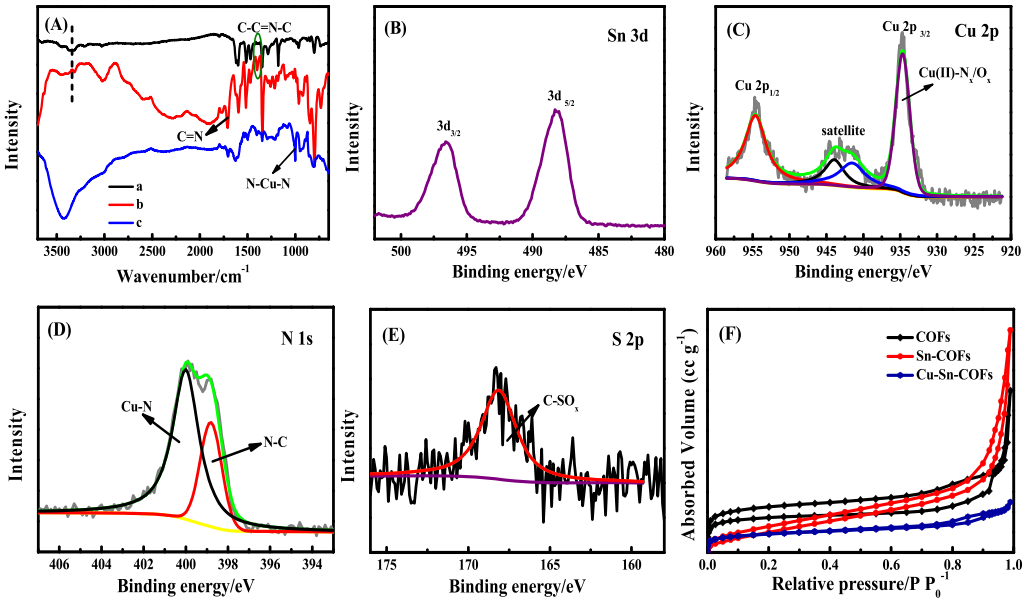

Fig. 2. (A) FT-IR spectra of TAPP (a), COFs (b) and Cu–Sn-COFs (c). The deconvoluted Sn 3d (B), Cu 2p (C), N 1s (D) and S 2p (E). (F) N_2 adsorption-desorption isotherms of COFs, Sn-COFs, and Cu–Sn-COFs.

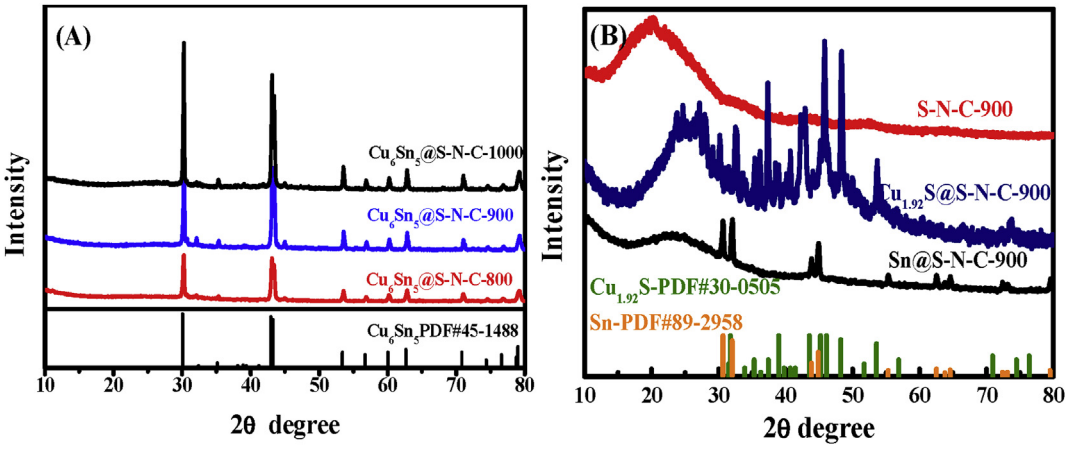

Fig. 3. (A) XRD patterns of Cu_6Sn_5@S–N–C-800, -900 and −1000. (B) XRD patterns of S–N–C-900, Sn@S–N–C-900 and $Cu_{1.92}$S@S–N–C-900.

clearer observation for Cu_6Sn_5 particles from high-resolution TEM (HRTEM) images (Fig. 4d,e) further verified the average particle size of about 2–10 nm, and the crystalline stripes corresponded to the (021) plane of Cu_6Sn_5 alloys with the lattice spacing of 0.34 nm. Element mapping and HADDF/STEM clearly illustrated the homogeneous distributions of Cu and Sn components on S, N-codoped carbons for Cu_6Sn_5@S–N–C-900 (Fig. 4f-i and 4l-n), agreeing with the results of XRD and TEM.

The special Cu–Sn-contained COF precursors played the important roles in the formation of pony Cu_6Sn_5 embedding on porous N and S-doped carbons. The large-angle XRD pattern of S–N–C-900 without Cu_6Sn_5 showed a strong graphite peak at around $2\theta = 20°$ (Fig. 3B). The pyrolysis of COFs without Cu and Sn at 900 °C only generated the low graphitization carbons. The single Cu-contained COFs derived hexagonal $Cu_{1.92}S$ particles (JSPDF No.30–0505) on S–N–C-900 after carbonization, affirmed by the characteristic diffraction peaks of $Cu_{1.92}S$ located at $2\theta = 30–80°$. After annealing COFs with Sn species, tetragonal Sn particles (JSPDF No.89–2958) on S–N–C-900 were obtained. In particular, the particle size of Sn and $Cu_{1.92}S$ even reached several micrometers presenting on their TEM images (Fig. 4j and k). It is evident that using Cu and Sn species in COFs together contributed to the generation of Cu_6Sn_5 nanoalloys with small particle size. Sn was often reported as the "co-catalyst" in Cu-based catalysts, helping metallic Cu to strong interacting with carbons [43]. The liquid Sn droplets might easily contact and react with Cu species at higher temperature, which facilitated the formation of intermetallic Cu_6Sn_5 alloys, other than $Cu_{1.92}S$. The high melting points and low mobility of Cu_6Sn_5 alloys made them become the smaller particles or encapsulated by carbon plates. Moreover, the porous organic frameworks also resulted into the fabrication of carbons with abundant porosities, which could separate or isolate liquid droplets of Sn or Cu_6Sn_5 and give small-size particles during cooling process. Combining these interactions generated the hybrid particles of pony Cu_6Sn_5 alloys and porous N–S–Cs.

The porosities of Cu_6Sn_5@S–N–Cs were further detected by N_2 adsorption-desorption measurement (Fig. 5A–C). The affluent porosities were expected to increase the exposure of active sites and

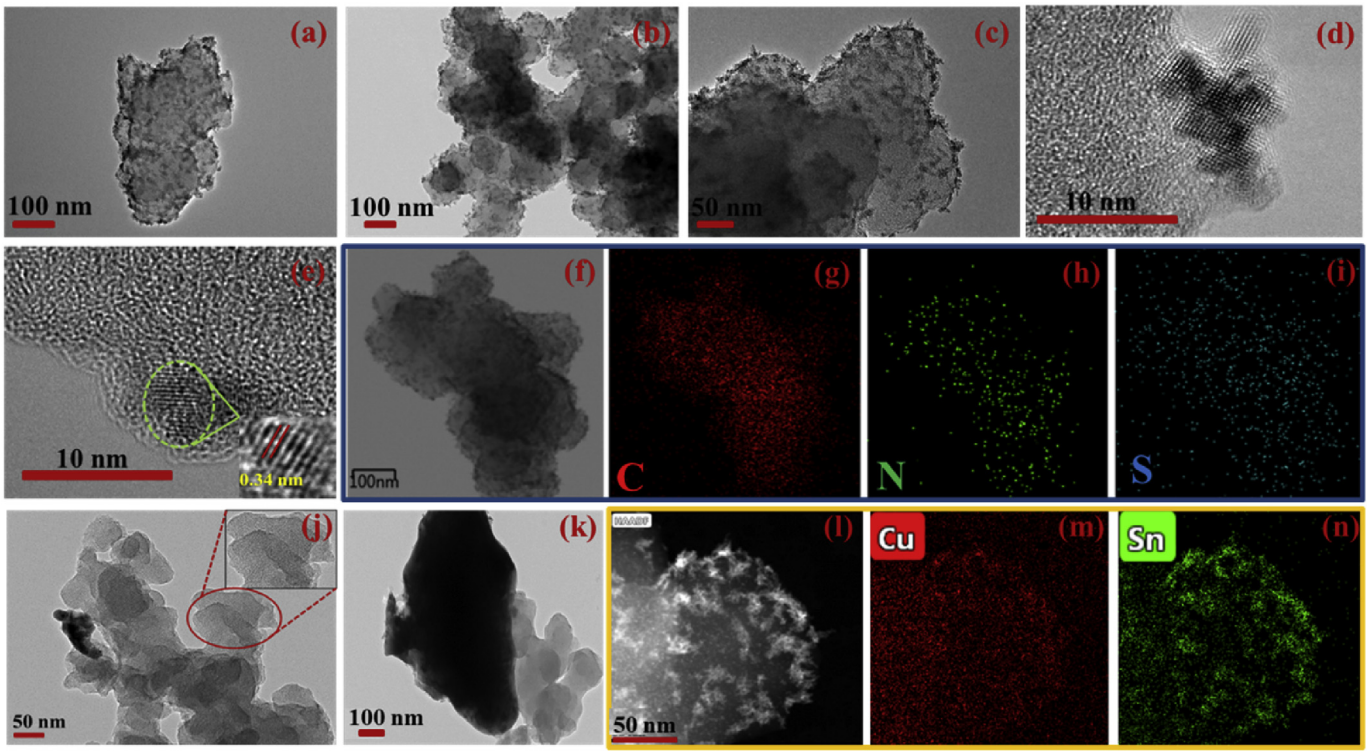

Fig. 4. TEM images of Cu_6Sn_5@S–N–C-900 (a–d). HRTEM images of Cu_6Sn_5@S–N–C-900 (e). STEM HADDF element mapping images of C (g), N (h),S (i) Cu (m), Sn (n). TEM images of Sn@S–N–C-900 (j) and $Cu_{1.92}$S@S–N–C-900 (k).

promote the mass transportation properties of Cu_6Sn_5@S–N–C. The isotherm curves of Cu_6Sn_5@S–N–Cs could be classified as a type I isotherm for microporous materials. There was an inconspicuous hysteresis loop at relative pressure (P/P_0) of 0.2–0.8 (Fig. 5A). An abrupt adsorption increase at high relative pressure above 0.95 P/P_0 was also observed. This should be ascribed to N_2 adsorption in the particles-stacking mesopores and macropores. Cu_6Sn_5@S–N–C-900 owned the highest BET specific surface area (S_{BET}) of 602 $m^2\ g^{-1}$ among the Cu_6Sn_5@S–N–Cs prepared at different temperatures. The micropores centred at 0.4–0.6 nm accounted for 74% of total surface area (Table 1). Sn@S–N–C-900 prepared at the same temperature also revealed type I isotherm with a BET surface area of 452 m^2/g, 150 m^2/g smaller than that of Cu_6Sn_5@S–N–C-900. For $Cu_{1.92}$S@S–N–C-900, it had its very lower surface area (40 $m^2\ g^{-1}$), owing to the formed large-size non-porous $Cu_{1.92}S$ particles with higher molecular mass (Fig. 4k and S4A). The pore analysis results demonstrated that Cu_6Sn_5@S–N–C-900 possessed the optimized pore properties after introducing Cu and Sn among these samples.

3.3. Surface ingredients and defects

The heteroatom-doping in carbon lattices often adjusted the electronic and chemical properties of carbons, and served as active sites for ORR. The defect level of S–N–C-900, Sn@S–N–C-900, $Cu_{1.92}$S@S–N–C-900 and Cu_6Sn_5@S–N–C-900 (Fig. 5D) have been detected by Raman spectroscopy. All Raman spectra exhibited two clear C–C adsorption signals at 1340 and 1579 cm^{-1}, corresponding to disordered sp^3 carbon (D band) and graphite sp^2 carbon (G band). The ratio (I_D/I_G) of peak intensity was 1.02 for Cu_6Sn_5@S–N–C-900, much higher than 0.99 of Sn@S–N–C-900, 0.96 of $Cu_{1.92}$S@S–N–C-900 and 0.93 of S–N–C-900. Introducing Cu and Sn into the COF precursors might contribute to the raising of O, N and S content on carbon surface and thus the improved doping levels of heteroatoms. Moreover, the electron conductivity of the as-prepared Cu_6Sn_5@S–N–C-900 was also investigated by the electrochemical impedance spectroscopy (EIS). On the basis of the equivalent circuit models, the R_{ct} values are 27.2, 35.6 and 40.3 for Cu_6Sn_5@S–N–C-900, Sn@S–N–C-900 and $Cu_{1.92}$S@S–N–C-900, respectively (Fig. S4B). Cu_6Sn_5@S–N–C-900 represented the lowest Rct value, indicating its higher electron transportation abilities. The higher conductivity of highly dispersed Cu_6Sn_5 nanoparticles could increase the electron transportation in carbon-based catalysts. Moreover, like the catalytic behavior of Fe and Co species in the carbonization of organic materials [49,50], Cu and Sn species might facilitate the graphitization of organic frameworks at higher pyrolysis temperature.

Chemical composition and elemental states on the surface of Cu_6Sn_5@S–N–C-900 were probed with XPS techniques. As shown in Fig. S2D, the XPS survey spectrum of Cu_6Sn_5@S–N–C-900 revealed distinctive peaks of Cu, Sn, S, N, O and C. It confirmed the successful introduction of Cu, Sn, N and S in the surface of Cu_6Sn_5@S–N–C-900. Two Cu (II) characteristic peaks of Cu $2p_{1/2}$ and $2p_{3/2}$ were found at binding energies of 954 and 934 eV (Fig. 5E), originating from Cu-N_x or SnO_x shells at the outside of Cu_6Sn_5 [44]. The additional signal locating at 932.9 eV was attributed to the appearance of Cu (0) [44], assigning to Cu (0) in Cu_6Sn_5 alloys. The high-resolution spectrum for Sn 3d in Cu_6Sn_5@S–N–C-900 could be deconvoluted into two peaks at 486.9 and 495.3 eV of Sn $3d_{5/2}$ and Sn $3d_{3/2}$, manifesting the formation of SnO_x on surface of Cu_6Sn_5 particles. The oxytropic properties made Sn easily oxidized to SnO_x layers at the surface of metal nanoparticles (Fig. 5F) [45], and the appearance of Sn–O signals could be also verified in O_{1s} spectrum (Fig. 5G). There were two XPS signals of Sn (0) species at 485.1 and 493.5 eV, corresponding to Sn(0) in Cu_6Sn_5 alloys.

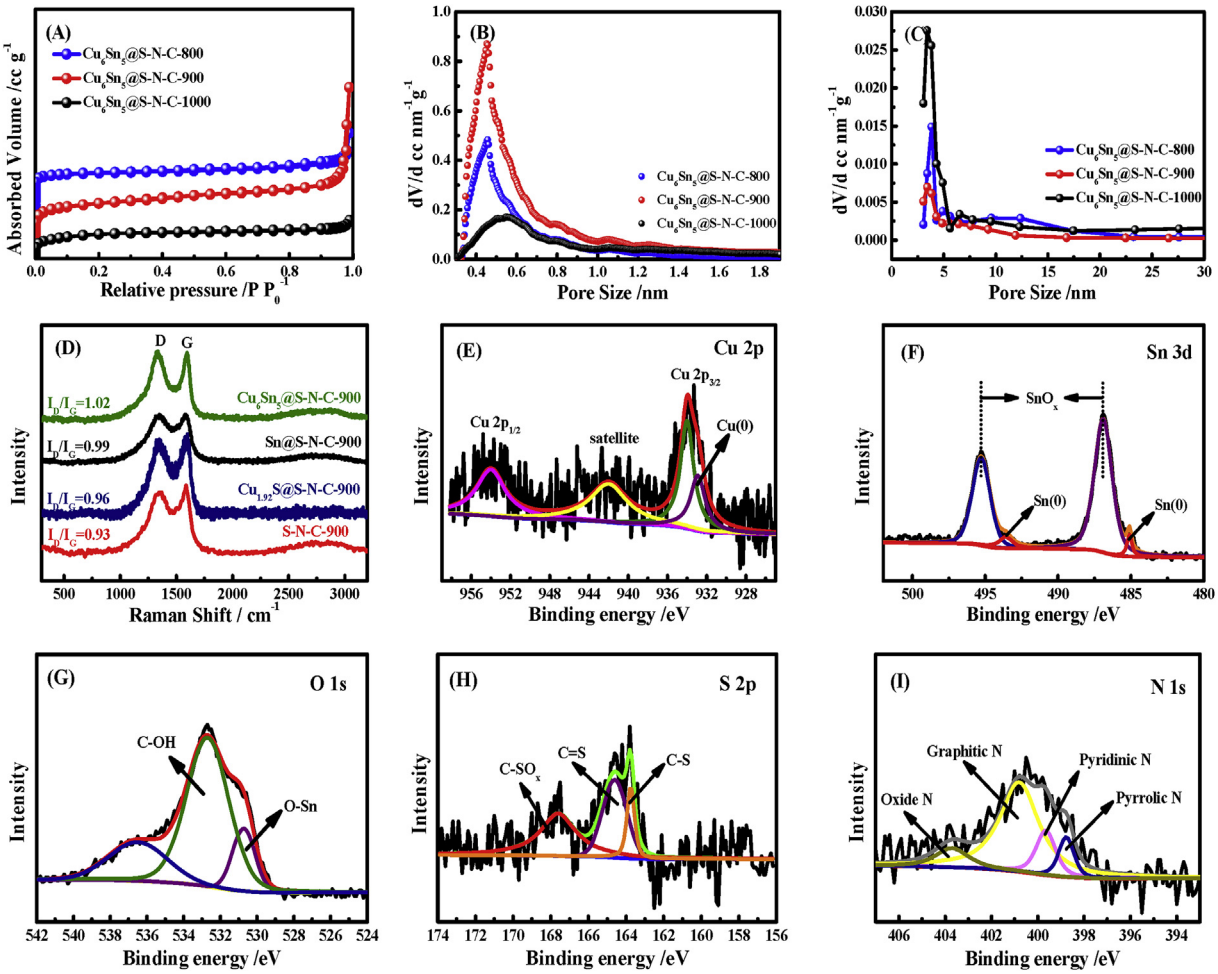

Fig. 5. N_2 adsorption-desorption isotherms (A) and corresponding HK (B) and BJH (C) pore distribution curves of Cu_6Sn_5@S−N−C-800, -900 and −1000. (D) Raman spectrum of S−N−C-900, $Cu_{1.92}S$@S−N−C-900, Sn@S−N−C-900 and Cu_6Sn_5@S−N−C-900. The deconvoluted Cu 2p (E), Sn 3d (F), O 1s (G), S 2p (H) and N 1s (I) of Cu_6Sn_5@S−N−C-900 XPS spectra.

Table 1
The textural parameters of Cu−Sn-COFs and Cu_6Sn_5@S−N−Cs

Samples	S_{BET} [m^2/g]	$S_{micropore}$ [m^2/g]	$S_{exteral}$ [m^2/g]	V_{total} [cc/g]	$V_{micropore}$ [m^2/g]	d_{HK} [nm]	d_{BJH} [nm]
Cu−Sn-COFs	162	74.5	87.5	0.192	0.060	0.490	3.80
Cu_6Sn_5@S−N−C-800	325	283	43.0	0.290	0.128	0.500	4.00
Cu_6Sn_5@S−N−C-900	602	448	154	0.720	0.242	0.450	4.00
Cu_6Sn_5@S−N−C-1000	230	194	36.0	0.160	0.095	0.550	4.00
Sn@S−N−C-900	452	280	172	0.60	0.19	0.44	3.40
$Cu_{1.92}S$@S−N−C-900	40	25	15	0.16	0.04	0.49	4.50

DMSO solvent left in Cu−Sn-COFs acts as S source of the as-prepared hybrid carbons, which led to the doping of S in carbon matrixes. The high-resolution S 2p peaks locating at t 163.7, 164.6 and 167.5 eV indicated the surface S atoms in the form of C−S, C═S, and C-SO_x (Fig. 5H) [31]. The existence of Cu or Sn sulphides in Cu_6Sn_5@S−N−C-900 could not be observed in the XPS measurement, consistent with the XRD results. The easily-formed Sn liquid droplets during high-temperature carbonization facilitated the formation of Cu_6Sn_5 alloys, instead of $Cu_{1.92}S$ particles. N 1s spectrum (Fig. 5I) was deconvoluted into four peaks, attributing to pyridinic N (398.7 eV), pyrrolic N (399.6 eV), graphitic N (400.8 eV) and oxide N (403.7 eV), respectively [46]. It could be clearly seen that pyridine-N and graphite-N are dominant N-types in Cu_6Sn_5@S−N−C-900. The XPS results further confirmed the formation of Cu_6Sn_5 alloys with thin SnO_x shells on the N−S−Cs. The little Cu-N_x species, N−S-doped carbons and Cu_6Sn_5@SnO_x-- activated carbon layers could also serve as the efficient active sites for ORR in Cu_6Sn_5@S−N−C-900.

3.4. Electrochemical properties of Cu_6Sn_5@S−N−C for ORR

Inspired by distinctive structure of as-prepared Cu_6Sn_5@S−N−Cs, their ORR electrocatalytic performance has been investigated in alkaline electrolytes. As shown in the Fig. 6A, a well-defined reduction peak was discovered in O_2-saturated KOH solution but was not observed in N_2-saturated electrolyte, affirming the prominent ORR activities of Cu_6Sn_5@S−N−C-900. Steady-state LSV curves of Cu_6Sn_5@S−N−C-800, -900 and −1000 were

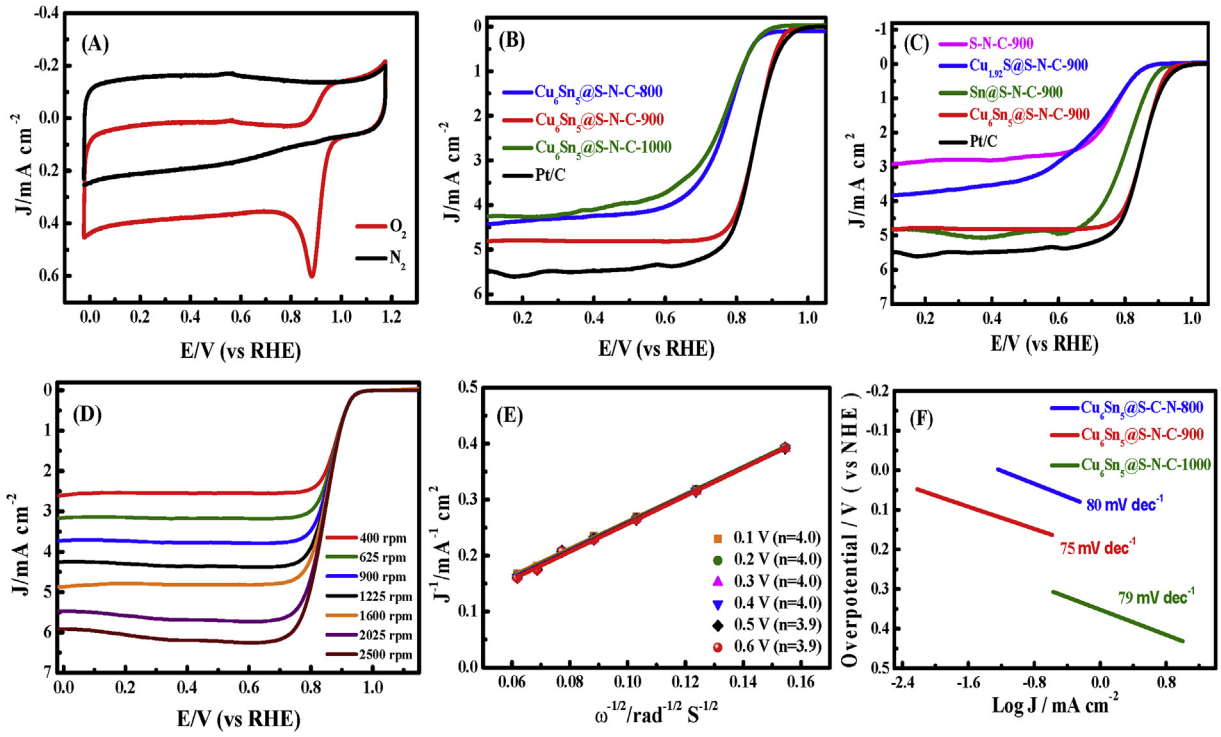

Fig. 6. (A) ORR CV conducted on Cu_6Sn_5@S–N–C-900 in 0.1 M KOH under O_2 or N_2-saturated atmosphere. (B) LSV curves on Cu_6Sn_5@S–N–C-800, -900,-1000 and Pt/C. (C) LSV conducted in O_2-saturated 0.1 M KOH of S–N–C-900, $Cu_{1.92}S$@S–N–C-900, Sn@S–N–C-900, Cu_6Sn_5@S–N–C-900 and Pt/C. (D) LSV curves recorded for Cu_6Sn_5@S–N–C-900 at different rotation rates in 0.1 M KOH. (E) K-L plots of J^{-1} versus $\omega^{-1/2}$ for Cu_6Sn_5@S–N–C-900 at different potentials. (F) Tafel plots of Cu_6Sn_5@S–N–C-800, -900 and −1000.

displayed in Fig. 6B. Cu_6Sn_5@S–N–C-900 possessed the most positive half-wave potential ($E_{1/2}$) of 0.86 V (vs RHE) among them, competitive to commercial Pt/C (0.86 V). This $E_{1/2}$ potential of Cu_6Sn_5@S–N–C-900 is also among the best Fe (or Co)-based ORR electrocatalysts, 20 mV higher than the previously reported Sn-contained electro-catalysts (Table S2). The elevating heat-treatment temperatures are often favorable to the graphitization of carbon and thus enhance the electron transportation properties. However, the mass-transportation properties and the density of active sites would often decrease with the sintering and degradation of heteroatoms in carbons at very high pyrolysis temperatures (Table S1). The balance results of these factors enabled Cu_6Sn_5@S–N–C-900 to be the most active for ORR among these Cu_6Sn_5@S–N–Cs. Moreover, Cu_6Sn_5@S–N–C-900 also testified more efficient ORR performance than metal-free S–N–C-900 (0.72 V), $Cu_{1.92}S$@S–N–C-900 (0.74 V), and Sn@S–N–C-900 (0.81 V) (Fig. 6C). The robust catalytic performance of Cu_6Sn_5@S–N–C-900 highlights the advantages of the formed small-size Cu_6Sn_5 nanoparticles strongly embedding on porous N and S-codoped carbons.

The ORR kinetics and reaction pathways of Cu_6Sn_5@S–N–C-900 were evaluated by LSV at different rotation rates in the range of 400–2500 rpm. With the increasing rotation rate (Fig. 6D), the limited diffusion current density of Cu_6Sn_5@S–N–C-900 increased linearly, because of the shortened O_2 diffusion distance in the electrolytes. The linear K-L plots at different potentials, obtained from the corresponding LSV plots (Fig. 6E) exhibited the first-order reaction kinetics toward the concentration of dissolved O_2. The calculated electron-transfer numbers (3.9–4.0) at different potentials indicated a four-electron-transfer pathway of ORR over Cu_6Sn_5@S–N–C-900. Cu_6Sn_5@S–N–C-900 also showed the smallest Tafel slope of 75 mV dec^{-1} among Cu_6Sn_5@S–N–Cs, close to commercial Pt/C (74 mV dec^{-1}) (Fig. 6F). This also suggested the better kinetic reaction pathway of Cu_6Sn_5@S–N–C-900.

It is well-known that Sn species supporting on carbon materials often reveal inferior ORR activities in $HClO_4$ due to its unstable and soluble properties. The efficient ORR activities of Sn-based electrocatalysts were yet rarely studied in acid. The CV curves of Cu_6Sn_5@S–N–C-900 revealed an obvious reduction peak at 0.72 V in O_2-saturated 0.1 M $HClO_4$, but disappeared in N_2-saturated electrolyte (Fig. 7A). Cu_6Sn_5@S–N–C-900 also embodied sizable limiting current density of 5.2 mA cm^{-2} and a half-wave potential of 0.67 V, manifesting the reasonable electrocatalytic activity in acidic media (Fig. 7B).

Durability and methanol-tolerance are another two crucial factors to represent the performance of ORR electro catalyst. The durability of Cu_6Sn_5@S–N–C-900 was investigated using continual CV scans (Figs. S5A and 5B) and Current-time (i-t) (Fig. 7C and D) chronoamperometric curves in O_2-saturated electrolytes. There were no remarkable changes happened in ORR CV curves in both media. In the i-t curves, the relative ORR current of about 93% over Cu_6Sn_5@S–N–C-900 electrodes in 0.1 M KOH and about 82% in 0.1 M $HClO_4$ solution still remained after 20 000 s. For Pt/C electrodes, the ORR relative current maintenance was about 65–75% at the same measurement conditions. The prepared Cu_6Sn_5@S–N–C-900 was found to exhibit higher durability during the ORR in both media. Unexpected durability of Cu_6Sn_5@S–N–C-900 might be attributed to the efficient embedding of Cu_6Sn_5 nanoalloys on N–S–Cs. In contrast, $Cu_{1.92}S$@S–N–C-900 (Fig. 7E) and Sn@S–N–C-900 (Fig. 7F) suffered distinct recession after durability test. The huge particles and uneven distribution of $Cu_{1.92}S$ and Sn particles might affect the effective supporting of them on carbons, and thus cause the easy degradation of active species. Moreover, after the addition of methanol, there was no great fluctuation in the ORR current density obtained over Cu_6Sn_5@S–N–C-900 (Fig. 8F). But an obvious current decline was observed for commercial Pt/C

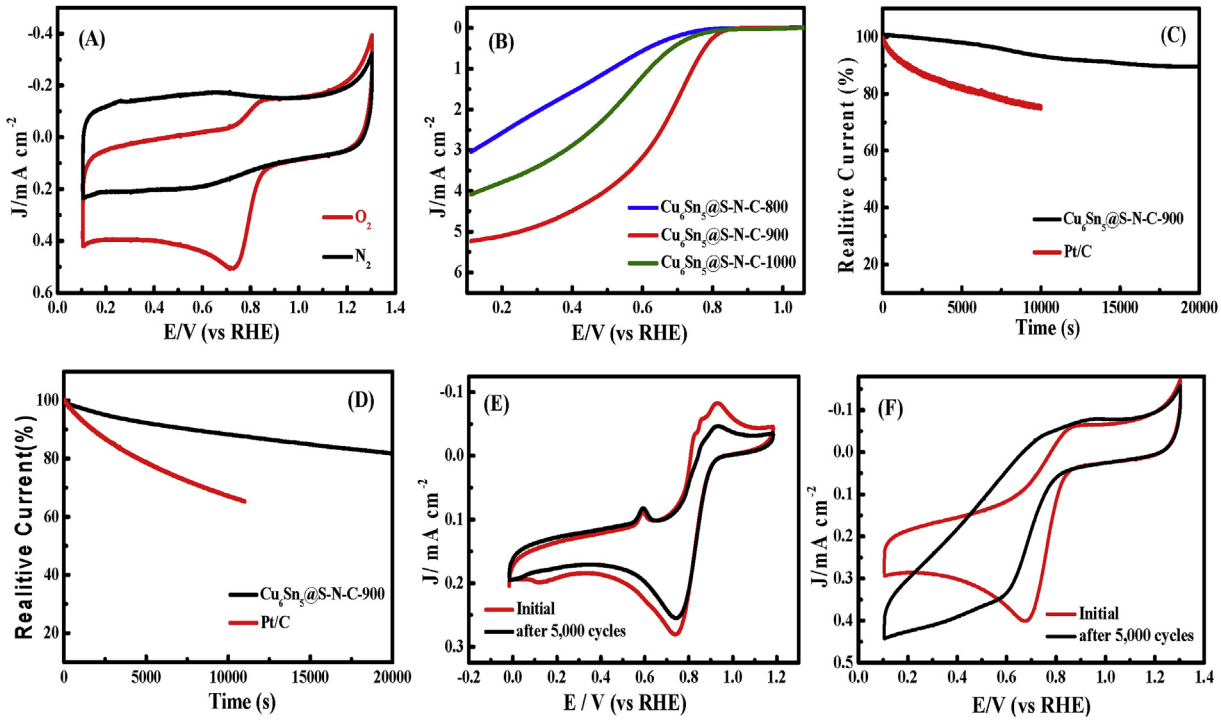

Fig. 7. (A) ORR CV performed on Cu_6Sn_5@S−N−C-900 in 0.1 M $HClO_4$ solution under O_2 or N_2-saturated atmosphere. (B) LSV curves on Cu_6Sn_5@S−N−C-800, -900 and −1000 in 0.1 M $HClO_4$. Current-time (i−t) chronoamperometric response of Cu_6Sn_5@S−N−C-900 and Pt/C in O_2-saturated 0.1 M KOH (C) and 0.1 M $HClO_4$ (D) at a rotation rate of 1600 rpm on the RRDE electrode. CVs after running for 5000 cycles in O_2-saturated 0.1 M KOH electrolyte for $Cu_{1.92}S$@S−N−C-900 (E), Sn@S−N−C-900 (F).

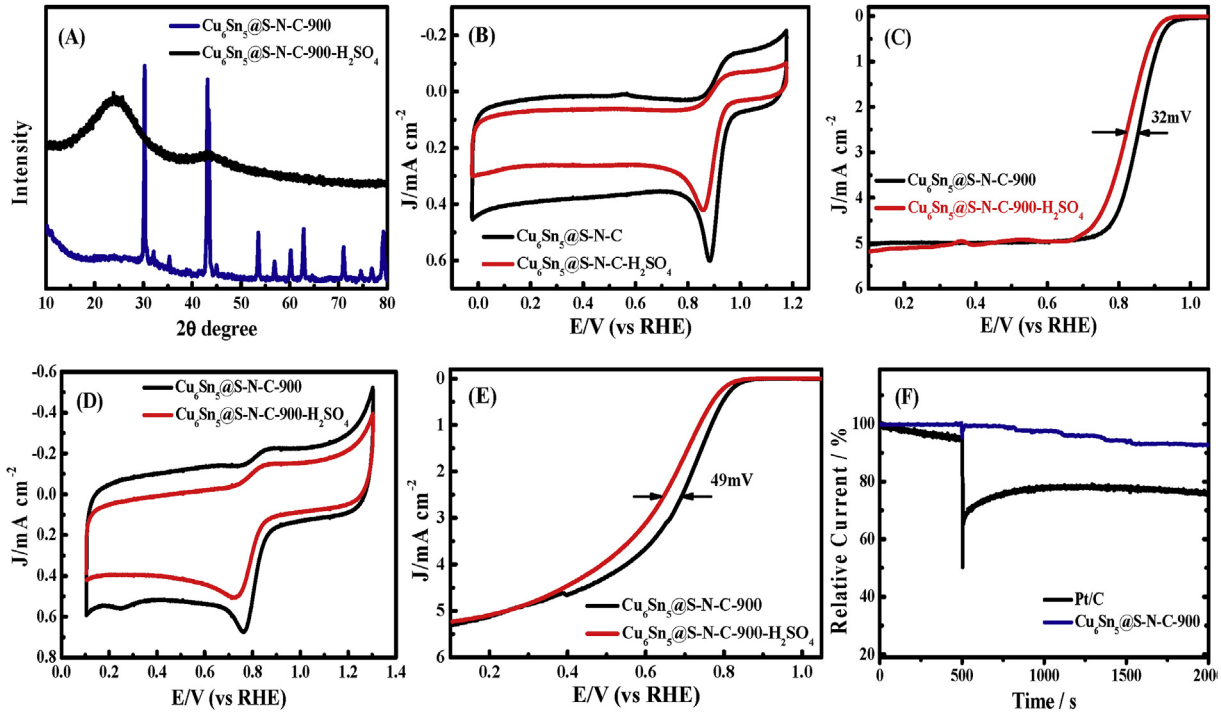

Fig. 8. (A) The large-angle XRD patterns of Cu_6Sn_5@S−N−C-900 and Cu_6Sn_5@S−N−C-900-H_2SO_4. CV and LSV curves of Cu_6Sn_5@S−N−C-900 and Cu_6Sn_5@S−N−C-900-H_2SO_4 conducted in 0.1 M KOH (B and C) and 0.1 M $HClO_4$ (D and E). (F) Current-time (i−t) chronoamperometric response of Cu_6Sn_5@S−N−C-900 and Pt/C-JM with the addition of methanol (3 wt %) in O_2-saturated 0.1 M KOH.

(20 wt %). It illustrated better durability and robust anti-methanol performance of Cu_6Sn_5@S−N−C-900.

To further detect the importance of Cu_6Sn_5 particles for ORR, 0.5 M concentrated sulfuric acid was used to etch off them. Conclusion could be drawn from XRD patterns that all peaks of Cu_6Sn_5 alloys disappeared after leaching (Fig. 8A). There were no

Cu_6Sn_5 particles with SnO_x on the porous carbons (Fig. S3D). When compared with the original Cu_6Sn_5@S–N–C-900, both the ORR onset potential and the half-wave potential of the residues decrease significantly (Fig. 8C and E). The great depression of catalytic performance of Cu_6Sn_5@S–N–C-900 could impute to dissolution of Cu_6Sn_5 nanoparticles with SnO_x shells and the evanescent synergistic effect. Moreover, electrochemically active surface area (ECSA) of Cu_6Sn_5@S–N–C-900 (451 cm^{-2}) was much higher than S–N–C-900 (55 cm^{-2}), $Cu_{1.92}S$@S–N–C-900 (193 cm^{-2}) and Sn@S–N–C-900 (372 cm^{-2}) (Fig. S6). These results demonstrated the importance of Cu_6Sn_5 with SnO_x shells for ORR. Pony Cu_6Sn_5 nanoalloys with SnO_x shells as the critical constituents were involved into ORR activity centers of Cu_6Sn_5@S–N–C-900. Similar to the enhancing ORR performance of hybrid carbons with Co_3O_4, Fe_3C and FeCo nanoparticles [37,38,47], Cu_6Sn_5@SnO_x could activate the tightly-contacted N–S-doped carbon layers, which acted as the higher active centers for ORR. Cu_6Sn_5@SnO_x might modulate the balance of adsorption and desorption of oxygen-related species on the surface of catalyst and improve the reduction kinetics of ORR.

3.5. Electrochemical lithium ion storage performance of Cu_6Sn_5@S–N–C-900

CuSn-based alloys have been demonstrated as the efficient anode materials for lithium ion storage. The pony-size and high dispersion state of Cu_6Sn_5 on N–S–Cs might help to improve their lithium ion storage performance. Fig. 9A exhibited the differential capacity plots (DCPs) for the first two cycles of the Cu_6Sn_5@S–N–C-900, showing that the anode behaviors are dominated by alloying-dealloying between Li and Cu_6Sn_5. It is reported that the lithiation/de-lithiation of Cu_6Sn_5 occurs mainly at potentials above 0.3 V, corresponding to Li-ion insertion into Cu_6Sn_5 in form of $Li_xCu_6Sn_5$ and Li_xSn [45,48].

The galvanostatic charge-discharge curves of Cu_6Sn_5@S–N–C-900 have been determined for the 1st and 2nd cycle in a voltage range of 0.01–1.5 V. As seen in Fig. 9B, the initial discharge and charge capacities were 905 and 413 mA h g^{-1} at a used current density of 50 mA g^{-1}. The potential plateaus observed in discharge curves mainly started from 0.48 V, while the charge curves illustrated several plateau at around 0.65 V. Moreover, the Cu_6Sn_5@S–N–C-900 electrode also exhibited an excellent rate capability (Fig. 9C). The reversible capacities at 50, 100, 200, 400, 800 and 1600 mA g^{-1} are 292, 230, 200, 175, 155 and 140 mAh g^{-1}. Thereby, Cu_6Sn_5 alloys clearly facilitated the transmission of electron and the charge-discharge capacity of Cu_6Sn_5@S–N–C-900 (Sn content is 18.7 wt % and Cu content is 8.3 wt %) are among the best Cu_6Sn_5@carbon electrode materials based on active metallic Sn (Table S3).

The long-time cycling measurement of Cu_6Sn_5@S–N–C-900 was also performed at a current density of 400 mA g^{-1} (Fig. 9D). Cu_6Sn_5@S–N–C-900 anode underwent a capacity drop during the 1st to 10th cycle. The capacity drop of lithium ion storage was commonly observed in previous studies of transition metal alloys or oxides as anode materials for LIBs [46,49,50]. It could be attributed to some irreversible reactions at the beginning experiment stages. However, during the following cycles, better cycling stability could be found for Cu_6Sn_5@S–N–C-900 electrode from the 100th to 300th cycle. The larger lithium ion storage capacities and long

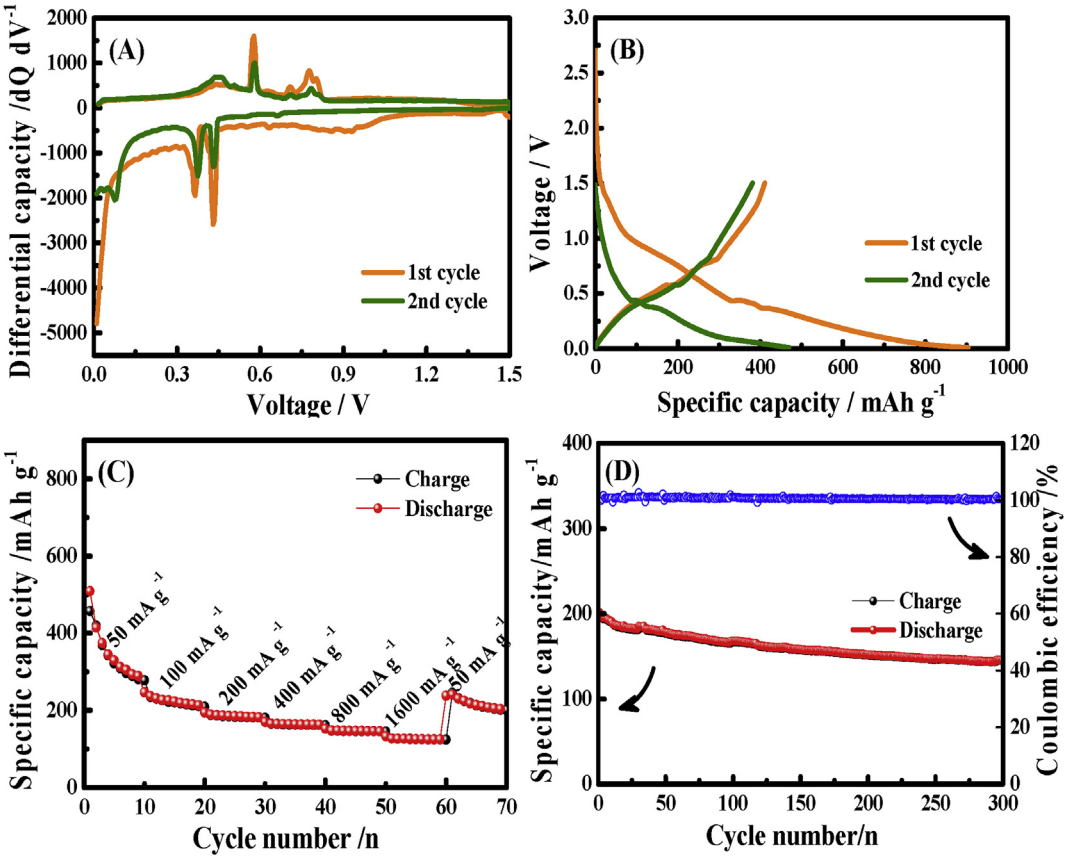

Fig. 9. (A) DCPs of Cu_6Sn_5@S–N–C-900. (B) Corresponding galvanostatic voltage profiles during the first two cycles at a current density of 50 mA g^{-1}. (C) Rate performance of Cu_6Sn_5@S–N–C-900. (D) Capacity-cycle number plot of the Cu_6Sn_5@S–N–C-900 electrodes cycled between 0.05 and 1.5 V at a current density of 0.4 A g^{-1}.

cycling stability of Cu_6Sn_5@S−N−C-900 demonstrated its promising application in LIBs. The efficient performance for lithium ion storage should be related to its unique local structures and components. The small-size and high dispersion of Cu_6Sn_5 on N−S−Cs with abundant porosities provided the convenient mass tunnels and high accessible Cu_6Sn_5 nanoparticles for lithium ion storage. The strongly coupling between Cu_6Sn_5 nanoalloys and N−S−C supports particles might effectively resist the exfoliation or aggregation of Cu_6Sn_5 from N−S−Cs and thus alleviate the destruction of Cu_6Sn_5 in lithium ion storage.

4. Conclusions

In summary, Cu_6Sn_5 nanoalloys with about 2−10 nm particle size supported on porous N and S-doped carbons were prepared by thermal conversion of one-pot synthesized Cu−Sn-contained covalent organic frameworks. This Fe-free and Pt-free Cu_6Sn_5@N−S−C-900 demonstrated highly efficient catalytic activities for ORR in both alkaline and acidic media. The ORR half-wave potential especially reached 0.86 V in 0.1 M KOH competitive to the best Fe (or Co)-based or Pt-based NPMCs [38,51]. Cu_6Sn_5@N−S−C-900 also displayed better durability and methanol-tolerance properties for ORR in both media, without the serious degradation in electrocatalysis. The electrochemical lithium ion storage capacity of Cu_6Sn_5@N−S−C also gave 905 mA h g^{-1} in an initial discharge at the optimized conditions, comparable to the best CuSn alloys. The carbonization of the designed COFs brought about the unique small-size Cu_6Sn_5 nanoalloys in a high dispersion state on carbons. This work not only provided an efficient synthesis strategy for the preparation of ultrafine Cu_6Sn_5 nanoparticles supporting on N−S-codoped carbons, but also presented a promising bifunctional electrode material for PEMFCs and lithium ion batteries.

Declaration of competing interest

The authors declare that they have no known competing financial interests or personal relationships that could have appeared to influence the work reported in this paper.

CRediT authorship contribution statement

Xiaoying Zhang: Investigation, Methodology, Writing - original draft. **Luyao Liu:** Investigation, Methodology. **Jiaxin Liu:** Investigation. **Tingting Cheng:** Methodology. **Aiguo Kong:** Conceptualization, Writing - review & editing, Supervision. **Yu Qiao:** Investigation. **Yongkui Shan:** Conceptualization.

Acknowledgments

The authors are grateful for financial support from the China National Natural Science Foundation, China (No.21303058) and Shanghai Municipal Natural Science Foundation (No.13ZR1412400).

Appendix A. Supplementary data

Supplementary data to this article can be found online at https://doi.org/10.1016/j.jallcom.2020.153958.

References

[1] Y.X. Liu, H.H. Wang, T.J. Zhao, Z.H. Xue, X.H. Li, J.S. Chen, Schottky barrier induced supported interface of electron-rich N-doped carbon and electron-deficient Cu: in-built lewis acid-base pairs for highly efficient CO_2 fixation, J. Am. Chem. Soc. 141 (2019) 38−41.
[2] Y. Cheng, X. Wu, J.P. Veder, L. Thomsen, S.P. Jiang, S. Wang, Tuning the electrochemical property of the ultrafine metal-oxide nanoclusters by iron phthalocyanine as efficient catalysts for energy storage and conversion, Energy Environ. Manag. 2 (1) (2019) 5−17.
[3] W. Liu, Y. Hou, Z. Lin, S.K. Yang, C.L. Yu, C.J. Lei, et al., Porous cobalt oxynitride nanosheets for efficient electrocatalytic water oxidation, ChemSusChem 11 (9) (2018) 1479−1485.
[4] Z. Fan, L. Zhang, D. Baumann, L. Mei, Y. Yao, X. Duan, et al., In situ transmission electron microscopy for energy materials and devices, Adv. Mater. 1900608 (2019) 1−22.
[5] Y. Qian, T. An, E. Sarnello, Z. Liu, T. Li, D. Zhao, Janus electrocatalysts containing MOF-derived carbon networks and NiFe-LDH nanoplates for rechargeable zinc−air batteries, ACS Appl. Energy Mater. 2 (3) (2019) 1784−1792.
[6] Z. Liang, C. Qu, W. Guo, R. Zou, Q. Xu, Pristine metal-organic frameworks and their composites for energy storage and conversion, Adv. Mater. 30 (37) (2018) 1−39, 1702891.
[7] X.Y. Yu, X.W. David Lou, Mixed metal sulfides for electrochemical energy storage and conversion, Adv. Energy Mater. 8 (3) (2018) 1−37, 1701592.
[8] J. Mao, J. Iocozzia, J. Huang, K. Meng, Y. Lai, Z. Lin, Graphene aerogels for efficient energy storage and conversion, Energy Environ. Sci. 11 (4) (2018) 772−799.
[9] Y. Zhao, L. Tao, W. Dang, L. Wang, M. Xia, B. Wang, et al., High-indexed PtNi alloy skin spiraled on Pd nanowires for highly efficient oxygen reduction reaction catalysis, Small 15 (17) (2019) 1−9, 1900288.
[10] S. Gupta, L. Qiao, S. Zhao, H. Xu, Y. Lin, S.V. Devaguptapu, et al., Highly active and stable graphene tubes decorated with FeCoNi alloy nanoparticles via a template-free graphitization for bifunctional oxygen reduction and evolution, Adv. Energy Mater. 6 (22) (2016) 1−12, 1601198.
[11] V.M. Dhavale, S. Kurungot, Cu−Pt nanocage with 3-D electrocatalytic surface as an efficient oxygen reduction electrocatalyst for a primary Zn−air battery, ACS Catal. 5 (3) (2015) 1445−1452.
[12] Z. Wang, H. Jin, T. Meng, K. Liao, W. Meng, J. Yang, et al., Fe, Cu-coordinated ZIF-derived carbon framework for efficient oxygen reduction reaction and zinc-air batteries, Adv. Funct. Mater. 28 (39) (2018) 1−8, 1802596.
[13] B. Chen, R. Li, G. Ma, X. Gou, Y. Zhu, Y. Xia, Cobalt sulfide/N,S codoped porous carbon core-shell nanocomposites as superior bifunctional electrocatalysts for oxygen reduction and evolution reactions, Nanoscale 7 (48) (2015) 20674−20684.
[14] N. Thiyagarajan, D. Janmanchi, Y.F. Tsai, W.H. Wanna, R. Ramu, S.I. Chan, et al., A carbon electrode functionalized by a tricopper cluster complex: overcoming overpotential and production of hydrogen peroxide in the oxygen reduction reaction, Angew. Chem., Int. Ed. Engl. 57 (14) (2018) 3612−3616.
[15] J. Kim, J.-E. Park, T. Momma, T. Osaka, Synthesis of Pd−Sn nanoparticles by ultrasonic irradiation and their electrocatalytic activity for oxygen reduction, Electrochim. Acta 54 (12) (2009) 3412−3418.
[16] J.B. Zhang, X.N. Li, S.L. Bai, R.X. Luo, A.F. Chen, Y. Lin, High-yield synthesis of SnO_2 nanobelts by water-assisted chemical vapor deposition for sensor applications, Mater. Res. Bull. 47 (11) (2012) 3277−3282.
[17] J. Chen, L. Yang, S. Fang, Z. Zhang, S.-i. Hirano, Facile fabrication of graphene/Cu_6Sn_5 nanocomposite as the high performance anode material for lithium ion batteries, Electrochim. Acta 105 (2013) 629−634.
[18] J.S. Thorne, J.R. Dahn, M.N. Obrovac, R.A. Dunlap, A comparison of sputtered and mechanically milled Cu_6Sn_5 + C materials for Li-ion battery negative electrodes, J. Power Sources 216 (2012) 139−144.
[19] W.-j. Cui, F. Li, H.-j. Liu, C.-x. Wang, Y.-y. Xia, Core−shell carbon-coated Cu_6Sn_5 prepared by in situ polymerization as a high-performance anode material for lithium-ion batteries, J. Mater. Chem. 19 (39) (2009) 7202−7220.
[20] L. Su, J. Fu, P. Zhang, L. Wang, Y. Wang, M. Ren, Uniform core−shell Cu_6Sn_5@C nanospheres with controllable synthesis and excellent lithium storage performances, RSC Adv. 7 (45) (2017) 28399−28406.
[21] H. Ying, W.Q. Han, Metallic Sn-based anode materials: application in high-performance lithium-ion and sodium-ion batteries, Adv. Sci. 4 (11) (2017) 1700298.
[22] X. Li, A. Dhanabalan, L. Gu, C. Wang, Three-Dimensional porous core-shell Sn@carbon composite anodes for high-performance lithium-ion battery applications, Adv. Energy Mater. 2 (2) (2012) 238−244.
[23] B. Ni, Y. Li, T. Chen, T. Lu, L. Pan, Covalent organic frameworks converted N, B co-doped carbon spheres with excellent lithium ion storage performance at high current density, J. Colloid Interface Sci. 542 (2019) 213−221.
[24] H. Huang, F. Li, Y. Zhang, Y. Chen, Two-dimensional graphdiyne analogue Co-coordinated porphyrin covalent organic framework nanosheets as a stable electrocatalyst for the oxygen evolution reaction, J. Mater. Chem. 7 (10) (2019) 5575−5582.
[25] Q. Lin, X. Bu, A. Kong, C. Mao, F. Bu, P. Feng, Heterometal-supported organic conjugate frameworks from alternating monomeric iron and cobalt metalloporphyrins and their application in design of porous carbon catalysts, Adv. Mater. 27 (22) (2015) 3431−3436.
[26] F. Kong, X. Fan, X. Zhang, L. Wang, A. Kong, Y. Shan, Soft-confinement conversion of Co-Salen-organic-frameworks to uniform cobalt nanoparticles supported within porous carbons as robust trifunctional electrocatalysts, Carbon 149 (2019) 471−482.
[27] M. Shao, A. Peles, K. Shoemaker, Electrocatalysis on platinum nanoparticles: particle size effect on oxygen reduction reaction activity, Nano Lett. 11 (9) (2011) 3714−3719.
[28] S. Lu, Y. Hu, S. Wan, R. McCaffrey, Y. Jin, H. Gu, et al., Synthesis of ultrafine and highly dispersed metal nanoparticles confined in a thioether-containing covalent organic framework and their catalytic applications, J. Am. Chem. Soc.

139 (47) (2017) 17082–17088.
[29] Z.Y. Wu, X.X. Xu, B.C. Hu, H.W. Liang, Y. Lin, L.F. Chen, Iron carbide nanoparticles encapsulated in mesoporous Fe-N-doped carbon nanofibers for efficient electrocatalysis, Angew. Chem. Int. Ed. 54 (28) (2015) 8179–8183.
[30] X. Fan, F. Kong, A. Kong, A. Chen, Z. Zhou, Y. Shan, Covalent porphyrin framework-derived Fe_2P@Fe_4N-supported nanoparticles supported in N-doped carbons as efficient trifunctional electrocatalysts, ACS Appl. Mater. Interfaces 9 (38) (2017) 32840–32850.
[31] F. Kong, X. Fan, A. Kong, Z. Zhou, X. Zhang, Y. Shan, Covalent phenanthroline framework derived FeS@Fe_3C composite nanoparticles embedding in N-S-codoped carbons as highly efficient trifunctional electrocatalysts, Adv. Funct. Mater. 28 (51) (2018) 1–14, 1803973.
[32] Q. Hong, H. Lu, Y. Cao, Improved oxygen reduction activity and stability on N, S-enriched hierarchical carbon architectures with decorating core-shell iron group metal sulphides nanoparticles for Al-air batteries, Carbon 145 (2019) 53–60.
[33] Z. Li, T. Yang, W. Zhao, T. Xu, L. Wei, J. Feng, et al., Structural modulation of Co catalyzed carbon nanotubes with Cu-Co bimetal active center to inspire oxygen reduction reaction, ACS Appl. Mater. Interfaces 11 (4) (2019) 3937–3945.
[34] G. Nam, J. Park, M. Choi, P. Oh, S. Park, M.G. Kim, et al., Carbon-Coated core-shell Fe-Cu nanoparticles as highly active and durable electrocatalysts for a Zn-air battery, ACS Nano 9 (6) (2015) 6493–6501.
[35] W. Wan, X. Liu, H. Li, X. Peng, D. Xi, J. Luo, 3D carbon framework-supported CoNi nanoparticles as bifunctional oxygen electrocatalyst for rechargeable Zn-air batteries, Appl. Catal., B 240 (2019) 193–200.
[36] M. Kuang, Q. Wang, P. Han, G. Zheng, Cu, Co-supported N-enriched mesoporous carbon for efficient oxygen reduction and hydrogen evolution reactions, Adv. Energy Mater. 7 (17) (2017) 1–8.
[37] T. Hu, Y. Wang, L. Zhang, T. Tang, H. Xiao, W. Chen, et al., Facile synthesis of PdO-doped Co_3O_4 nanoparticles as an efficient bifunctional oxygen electrocatalyst, Appl. Catal., B 243 (2019) 175–182.
[38] H. Wang, F.X. Yin, N. Liu, R.H. Kou, X.B. He, C.J. Sun, et al., Engineering Fe–Fe_3C@Fe–N–C active sites and hybrid structures from dual metal–organic frameworks for oxygen reduction reaction in H_2-O_2 fuel cell and Li–O_2 battery, Adv. Funct. Mater. 29 (23) (2019) 1–11.
[39] G. Derrien, J. Hassoun, S. Panero, B. Scrosati, Nanostructured Sn–C composite as an advanced anode material in high-performance lithium-ion batteries, Adv. Mater. 19 (17) (2007) 2336–2340.
[40] I.M. Costa, Y.N. Colmenares, P.S. Pizani, E.R. Leite, A.J. Chiquito, Sb doping of VLS synthesized SnO_2 nanowires probed by Raman and XPS spectroscopy, Chem. Phys. Lett. 695 (2018) 125–130.
[41] W. Wu, L. Zhan, W. Fan, J. Song, X. Li, Z. Li, et al., Cu-N dopants boost electron transfer and photooxidation reactions of carbon dots, Angew. Chem., Int. Ed. Engl. 54 (22) (2015) 6540–6544.
[42] Y. Ni, Z. Chen, F. Kong, Y. Qiao, A. Kong, Y. Shan, Space-confined synthesis of multilayer Cu-N-doped graphene nanosheets for efficient oxygen electroreduction, Dalton Trans. 46 (26) (2017) 8586–8592.
[43] Z. Zhang, Z.L. Wang, X. Lu, Multishelled Si@Cu microparticles supported on 3D Cu current collectors for stable and binder-free anodes of lithium-ion batteries, ACS Nano 12 (4) (2018) 3587–3599.
[44] S. Zhang, C. Zhao, Y. Liu, W. Li, J. Wang, G. Wang, et al., Cu doping in CeO_2 to form multiple oxygen vacancies for dramatically enhanced ambient N_2 reduction performance, Chem. Commun. 55 (20) (2019) 2952–2955.
[45] R. Hu, G.H. Waller, Y. Wang, Y. Chen, C. Yang, W. Zhou, et al., Cu_6Sn_5@SnO_2–C nanocomposite with stable core/shell structure as a high reversible anode for Li-ion batteries, Nanomater. Energy 18 (2015) 232–244.
[46] F.F. Cao, J.W. Deng, S. Xin, H.X. Ji, O.G. Schmidt, L.J. Wan, et al., Cu-Si nanocable arrays as high-rate anode materials for lithium-ion batteries, Adv. Mater. 23 (38) (2011) 4415–4420.
[47] X. Fu, Y. Liu, X. Cao, J. Jin, Q. Liu, J. Zhang, FeCo–N_x supported graphene as high performance catalysts for oxygen reduction reaction, Appl. Catal., B 130–131 (2013) 143–151.
[48] H.S. Hwang, T. Yoon, J. Jang, J.J. Kim, J.H. Ryu, S.M. Oh, Carbon fabric as a current collector for electroless-plated Cu_6Sn_5 negative electrode for lithium-ion batteries, J. Alloys Compd. 692 (2017) 583–588.
[49] X.H. Huang, X.H. Xia, Y.F. Yuan, F. Zhou, Porous ZnO nanosheets grown on copper substrates as anodes for lithium ion batteries, Electrochim. Acta 56 (14) (2011) 4960–4965.
[50] C. Yan, G. Chen, X. Zhou, J. Sun, C. Lv, Template-based engineering of carbon-doped Co_3O_4 hollow nanofibers as anode materials for lithium-ion batteries, Adv. Funct. Mater. 26 (9) (2016) 1428–1436.
[51] X. Hu, G. Wang, B. Wang, X. Liu, H. Wang, Co_3Sn_2/SnO_2 heterostructures building double shell micro-cubes wrapped in three-dimensional graphene matrix as promising anode materials for lithium-ion and sodium-ion batteries, Chem. Eng. J. 355 (2019) 986–998.